Fuel 334 (2023) 126771

Contents lists available at ScienceDirect

Fuel

journal homepage: www.elsevier.com/locate/fuel

Full Length Article

Effect of morphology and simultaneous sulfation on Fe doped CeO_2 for selective catalytic reduction of NO_x with NH_3

Jinxiu Wang [a,b,*], Yuqiu Liu [a,b], Xianfang Yi [a,b], Yanting Chen [a], Yanke Yu [c], Jinsheng Chen [a,b,*]

[a] Center for Excellence in Regional Atmospheric Environment, and Key Lab of Urban Environment and Health, Institute of Urban Environment, Chinese Academy of Sciences, Xiamen 361021, PR China
[b] University of Chinese Academy of Sciences, Beijing 100049, PR China
[c] Department of Environmental Science and Engineering, School of Energy and Power Engineering, Xi'an Jiaotong University, Xi'an 710049, PR China

ARTICLE INFO

Keywords:
SCR
Fe doping
Nanorod
Sulfate
Oxygen vacancy
Crystal planes

ABSTRACT

Researchers have been developing novel environment-friendly NH_3-SCR catalysts for controlling NO_x emission from fossil fuel combustion. Fe doped CeO_2 catalysts with nanorod, nanocube and nanopolyhedron shape were synthesized and sulfation was conducted on porous nanorod simultaneously. Their NO_x conversions were in sequence of sulfated porous nanorod (S-$FeCeO_x$) > nanorod (R-$FeCeO_x$) > nanopolyhedron (P-$FeCeO_x$) > nanocube (C-$FeCeO_x$) and presented distinct morphology dependence. S-$FeCeO_x$ catalyst possessed above 95 % NO_x conversion and nearly 100 % N_2 selectivity in very high gas hourly space velocity of 240, 000 $mL{\cdot}g^{-1}{\cdot}h^{-1}$ at 275–400 °C. The sequence of BET specific surface area was: P-$FeCeO_x$ > R-$FeCeO_x$ > S-$FeCeO_x$ > C-$FeCeO_x$ and thus the change of physical adsorption capacity may be not the main reason for high SCR catalytic activity of S-$FeCeO_x$ and R-$FeCeO_x$. Fe doping and sulfation induced porous nanorod shape with preferentially exposed {110} faces, most oxygen vacancy defect sites and highest surface chemisorbed oxygen ratio, which contributed to the highest NO_x conversion of S-$FeCeO_x$. Fe doping mainly increased strong acid sites, and surface sulfate species significantly increased Brønsted acid sites promoting NH_3 adsorption and suppressed NO_x adsorption on S-$FeCeO_x$ catalyst, beneficial to both high NO_x conversion and low N_2O formation on it. R-$FeCeO_x$ catalyst mainly followed Langmuir-Hinshelwood mechanism, while SCR reaction mechanism was changed by sulfation and S-$FeCeO_x$ catalyst mainly followed Eley-Rideal mechanism.

1. Introduction

Selective catalytic reduction of NO_x with ammonia (NH_3-SCR) technique in high efficiency is applied widely in controlling NO_x emission causing photochemical smog, ozone depletion, acid rain and haze. To remove NO_x from fossil fuel combustion, the industrial NH_3-SCR reaction is usually catalyzed by V_2O_5–WO_3 (or MoO_3)/TiO_2 at 300–400 °C. However, vanadium-based NH_3-SCR catalysts show toxicity of vanadium, narrow working temperature range and low efficiency at below 300 °C [1,2]. Therefore, many researchers have been devoting to the development of efficient and environment-friendly NH_3-SCR catalysts with wide working temperature range [3–5].

The high surface acidity and suitable redox ability both play significant roles in SCR activity. Generally, CeO_2 is an acid based substance, which has lots of Lewis acid sites and a few Brønsted acid sites. CeO_2 also possesses good reducibility because it stores and releases oxygen via the redox shift between Ce^{4+} and Ce^{3+}. Recent studies have indicated that a few novel NH_3-SCR catalysts with CeO_2 as the main active component or promoter perform high efficiency [6,7]. However, pristine CeO_2 catalyst facilitates side reactions of NH_3 oxidation, which is adverse to its NH_3-SCR performance [8]. Metal doping, such as Mn, Fe, V, Co and Ti, is considered an effective approach to improve the catalytic activity of CeO_2 [9–14]. Iron oxides as NH_3-SCR catalysts have been investigated in recent years due to their environmentally friendly properties and high thermal stability. They show excellent NH_3-SCR activity, high N_2 selectivity, and passable tolerance to H_2O and SO_2 at low temperatures [15]. Wang et al. prepared the mesoporous Fe doped CeO_2 catalyst and the Fe-Ce solid solution formed with low Fe addition via a vacancy compensation mechanism, which remarkably increased oxygen vacancies and then its catalytic performance [16]. Therefore, Fe doping

* Corresponding authors at: Center for Excellence in Regional Atmospheric Environment, and Key Lab of Urban Environment and Health, Institute of Urban Environment, Chinese Academy of Sciences, Xiamen 361021, PR China.
E-mail addresses: jxwang@iue.ac.cn (J. Wang), jschen@iue.ac.cn (J. Chen).

https://doi.org/10.1016/j.fuel.2022.126771
Received 18 July 2022; Received in revised form 19 October 2022; Accepted 13 November 2022
Available online 23 November 2022

may improve the NH_3-SCR activity of CeO_2 effectively, economically and environmentally benignly.

Moreover, CeO_2 nanocrystals expose different crystal faces in their surfaces depending on morphology, and hence CeO_2 and metal oxides/CeO_2 composite present morphology-dependent surface catalysis and chemistry. CeO_2 in the cubic fluorite structure has {111}, {100} and {110} low-index crystal faces. CeO_2 nanocrystals with various structures, such as cubes, polyhedra, octahedra and rods, have been synthesized successfully and studied in catalytic reactions [17]. CeO_2 cubes and octahedra are mainly enclosed by six {100} and eight {111} faces, respectively, although other low-index crystal faces may exist on their edges and corners owing to the morphological imperfections [17,18]. The exposed crystal faces on CeO_2 rods depend on the specific synthesis conditions such as calcination temperature and Ce precursors, and CeO_2 rods are enclosed commonly by {110} and {100} crystal faces and sometimes by {111} and {100} crystal faces [19,20]. Zhang et al. studied VO_x/CeO_2 catalysts, which employ CeO_2 nanorods, nanocubes, and nanopolyhedrons (NPs) with predominately exposed {110}, {100}, and {111} faces as supports. The excellent SCR activity of V-CeO_2-NPs is related to the exposed {111} faces [21]. Wu et al. further studied highly dispersed MnO_x-decorated VO_x/CeO_2 catalysts, and their SCR catalytic activity is in the sequence of VO_x-MnO_x/CeO_2-R (rod) > VO_x-MnO_x/CeO_2-P (polyhedra) > VO_x-MnO_x/CeO_2-C (cube). CeO_2 {110} face and surface oxygen vacancies promote significantly the NH_3-SCR activity [10]. Han et al. reported that Fe_2O_3/CeO_2{110} shows visibly higher NO conversion than pristine CeO_2{110} and Fe_2O_3/CeO_2{111} [22]. Therefore, the origin of the facet-dependent CeO_2 effect is still under debate and it is meaningful to study Fe doped CeO_2 catalysts with different morphologies to design efficient catalyst for NH_3-SCR reaction. Besides metal doping and morphology control, it is probable to obtain superior ceria-based NH_3-SCR catalysts by improving their acidity and then NH_3 adsorption and activation. Some studies demonstrated that sulfation treatment could facilitate the formation of sulfates on CeO_2 surface, which generate abundant Brønsted acid sites. Moreover, there are researches on sulfated CeO_2 deNO_x catalysts with different morphologies. Ma et al. reported sulfation treatment improved largely NO_x conversions of CeO_2 cubes and nanospheres by the impregnation in $(NH_4)_2SO_4$, and sulfated CeO_2 cubes performed better than sulfated CeO_2 nanospheres at 200–500 °C [8,23]. Chen et al. prepared sulfated CeO_2 nanorods, nanospheres, nanocubes and spindles with flowing SO_2, and they exhibit high catalytic activity and strong tolerance to SO_2. The effect of sulfation on nano-CeO_2 is obviously dependent on morphology and sulfated CeO_2 in rod shape shows the optimal NO_x conversion [24]. The common methods of introducing SO_4^{2-} are impregnation of H_2SO_4 or $(NH_4)_2SO_4$, or heat treatment with flowing SO_2 or H_2S gas [23,25–27]. To obtain sulfated CeO_2 via these methods usually needs two steps including the synthesis of CeO_2 and the sulfation treatment. It is significant to obtain sulfated CeO_2 based catalysts by one-step synthesis. Besides, there is no report on sulfated Fe doped CeO_2 deNO_x catalysts with special morphologies. Therefore, it is meaningful to study the effect of morphology and sulfation by one-step synthesis on Fe doped CeO_2 for selective catalytic reduction of NO_x with NH_3.

In this work, Fe doped CeO_2 with various shapes including nanorod, nanocube and nanopolyhedron were synthesized and a sulfated Fe doped CeO_2 with porous nanorod shape can be obtained by one-step hydrothermal synthesis using Na_2S as precipitant. The difference in their catalytic activity and physicochemical properties resulting from shapes and sulfation were systematically investigated and analyzed. The correlations between their surface properties and reactivity were studied and their reaction mechanisms were further explored.

2. Experiment

2.1. Preparation of samples

Fe doped CeO_2 samples with different shapes including nanorod, nanocube and nanopolyhedron were prepared via the following hydrothermal methods evolved from reported methods [18,28,29]. Briefly, 20 mL of solution containing 0.32 mmol of $Fe(NO_3)_3{\cdot}9H_2O$ and 6 mmol of cerium source (the molar ratio Fe/(Fe + Ce) = 0.05) was firstly poured into 60 mL of alkali solution as precipitant. The produced turbid liquid was then stirred for 30 min with magnetic stirrer and transferred into a 100 mL Teflon bottle which was then put in a stainless steel vessel autoclave. Following that, the autoclave was sealed tightly and with a hydrothermal treatment at 180 °C for 12 h in a electrothermal blowing dry box. Finally, the produced precipitate after hydrothermal reaction was collected and washed by centrifugation with deionized water thoroughly, followed by drying at 60 °C for 20 h and calcination at 450 °C for 3 h at the ramping rate in 5 °C/min. Fe doped CeO_2 samples in rod, cube and polyhedron shape were abbreviated as R-$FeCeO_x$, C-$FeCeO_x$ and P-$FeCeO_x$. Sulfated Fe doped CeO_2 nanorod sample was abbreviated as S-$FeCeO_x$. The cerium sources and alkali sources (amount) used in the above synthesis of R-$FeCeO_x$, C-$FeCeO_x$, P-$FeCeO_x$ and S-$FeCeO_x$ catalyst were cerium acetate and NaOH (0.42 mol), cerium nitrate and NaOH (0.42 mol), cerium nitrate and $NH_3{\cdot}H_2O$ (0.08 mol), cerium acetate and Na_2S (0.018 mol), respectively. The corresponding R-CeO_2, C-CeO_2, P-CeO_2 and S-CeO_2 catalysts also were synthesized by the above procedure without adding Fe.

2.2. Catalytic activity test

The catalytic activity of these prepared samples was evaluated with a lab testing unit comprising gases supply, preheating and mixing gases furnace, a quartz tube fixed-bed reactor and a gas analyzer. In each test, 0.2 g of catalyst with size 0.28–0.45 mm was placed in the middle of quartz reactor (dimeter ϕ 6.0 mm) and sealed by quartz wool. The reaction feed gas composition contained 500 ppm NO_x (≈ 493 ppm NO and 7 ppm NO_2), 500 ppm NH_3, 5 vol% O_2, 5 vol% H_2O (when used), 50 ppm SO_2 or 200 ppm SO_2 (when used) and N_2 as the balance gas. The concentrations of NO, NH_3, NO_2, N_2O and SO_2 were determined by a Fourier transform infrared (FTIR) gas analyzer (Antaris IGS, Thermo Fisher Scientific).

The NO_x conversion and N_2 selectivity were calculated by the following expressions.

$$NO_x\ \text{Conversion}\ (\%) = \left(1 - \frac{[NO_x]_{out}}{[NO_x]_{in}}\right) \times 100\% \quad (1)$$

$$N_2\ \text{Selectivity}\ (\%) = \left(1 - \frac{2[N_2O]_{out}}{[NO_x]_{in} + [NH_3]_{in} - [NO_x]_{out} - [NH_3]_{out}}\right) \times 100\% \quad (2)$$

$[NO_x]$ represented the total concentration of NO and NO_2. $[NO_x]_{in}$, $[NO_x]_{out}$, $[NH_3]_{in}$, $[NH_3]_{out}$ and $[N_2O]_{out}$ represented the inlet and outlet gas concentration, respectively.

2.3. Characterization

The physicochemical properties of prepared samples were characterized by X-ray diffraction (XRD), N_2 adsorption–desorption, X-ray fluorescence spectrometer (XRF), scanning electron microscope with energy dispersive spectrometer (SEM-EDS), transmission electron microscopy (TEM), Raman spectra, X-ray photoelectron spectroscopy (XPS), temperature programmed desorption of NH_3 (NH_3-TPD) and temperature programmed reduction of H_2 (H_2-TPR) and *in situ* diffuse reflectance infrared fourier transform spectroscopy (*in situ* DRIFTS). The characterization method was similar to reference [11] and more details were described in the supplementary material.

Table 1
The atomic ratios in $FeCeO_x$ samples detected by EDS and XRF.

Sample	Fe/(Fe + Ce) by EDS	Fe/(Fe + Ce) by XRF	S/(Fe + Ce) by XRF
R-$FeCeO_x$	0.048	0.058	–
C-$FeCeO_x$	0.052	0.060	–
P-$FeCeO_x$	0.045	0.051	–
S-$FeCeO_x$	0.048	0.049	0.046

3. Results and discussion

3.1. Composition and structure

3.1.1. The element composition

The element composition was detected by XRF and EDS, and the results are listed in Table 1. The determined atomic ratio of Fe/(Fe + Ce) in R-$FeCeO_x$, C-$FeCeO_x$, P-$FeCeO_x$ and S-$FeCeO_x$ all approached the design value 0.05. S element could be detected in S-$FeCeO_x$ sample by XRF and S/(Fe + Ce) value was 0.046. The simultaneous sulfation and Fe doping into CeO_2 can be obtained in S-$FeCeO_x$ sample by one-step hydrothermal synthesis using Na_2S as precipitant.

3.1.2. XRD patterns

The XRD patterns of the prepared catalysts and their partial magnification are shown in Fig. 1. The diffraction peaks of all samples matched CeO_2 in a cubic fluorite structure (JCPDS 01–081-0792) and characteristic peaks of iron oxide and sulfate phases were not observed. The sequence in the crystallinity of Fe doped CeO_2 catalysts was as follows: C-$FeCeO_x$ > R-$FeCeO_x$ > P-$FeCeO_x$ > S-$FeCeO_x$, which was the same as that of CeO_2 catalysts. The diffraction peaks of $FeCeO_x$ catalysts became lower and wider than that of CeO_2 catalysts, indicating that Fe doping decreased the crystallinity of CeO_2. Besides, the diffraction angle (2θ) of the main peak attributed to (1 1 1) crystal plane on each $FeCeO_x$ catalyst shifted to the larger values than that of the corresponding CeO_2 catalyst (clearly shown in Fig. 1b). Therefore, Fe doping (5.0 at%) into CeO_2 decreased the lattice parameters. The results demonstrated the solid solution of iron-cerium oxide might form in $FeCeO_x$ catalysts by the substitution of Fe for Ce in the CeO_2 lattice [30]. The shift of S-$FeCeO_x$ was less than that of other $FeCeO_x$ catalysts, which indicated S may also be into CeO_2 lattice. Ion doping in the oxide can generate oxygen vacancies due to destroying the long-term periodic order of the lattice oxygen. The dopant ions with a low valence state replace the original metal ions of the oxide, and subsequently oxygen vacancies are formed to rebalance the charge [31]. S-$FeCeO_x$ catalyst showed the lowest crystallinity, which indicated the simultaneous Fe doping and sulfation further decreased the crystallinity. The lower crystallinity means the smaller grain size, larger BET specific surface area and more lattice defects, which may benefit the higher SCR catalytic activity [31,32].

3.1.3. The morphology

SEM images of the prepared catalysts were shown in Fig. S1. R-$FeCeO_x$, C-$FeCeO_x$, P-$FeCeO_x$ and S-$FeCeO_x$ samples presented nanorod, nanocube, nanopolyhedron and nanorod shape, respectively. The nanocube and nanopolyhedron of C-$FeCeO_x$ and P-$FeCeO_x$ were smaller than that of C-CeO_2 and P-CeO_2, which indicated Fe doping decreased their size. S-CeO_2 was composed of nanoparticles and Fe doping significantly changed its morphology. Fig. S2 shows the EDS-mapping images of elements in S-$FeCeO_x$ catalyst, confirming the uniform distribution of Fe. The above results demonstrated Fe doping affected the morphology of CeO_2 catalysts with various shapes to different degrees.

TEM images and high resolution transmission electron microscopy (HRTEM) images of R-$FeCeO_x$, C-$FeCeO_x$, P-$FeCeO_x$ and S-$FeCeO_x$ were

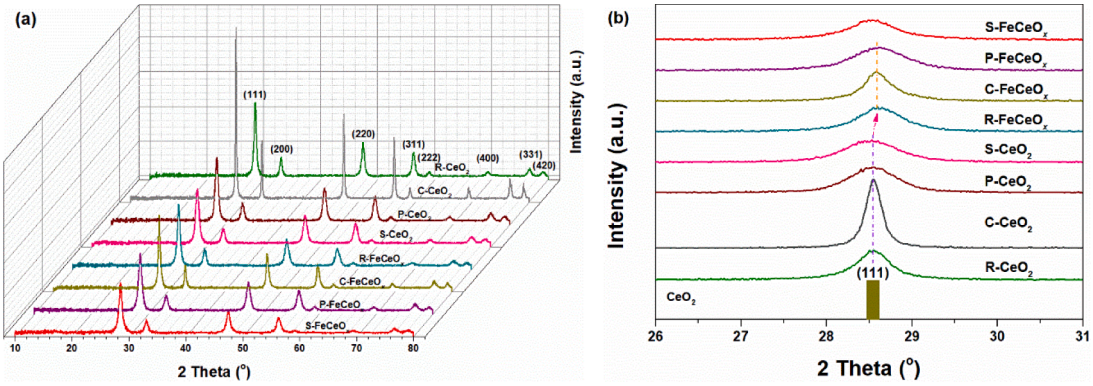

Fig. 1. (a) XRD patterns and (b) its partial magnification of the prepared catalysts.

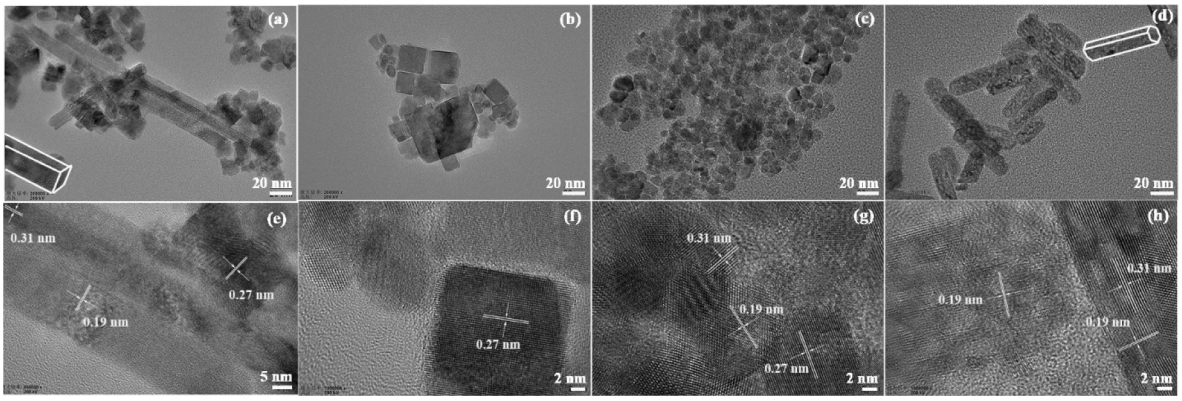

Fig. 2. TEM and HRTEM images of (a) (e) R-$FeCeO_x$, (b) (f) C-$FeCeO_x$, (c) (g) P-$FeCeO_x$, (d) (h) S-$FeCeO_x$ catalyst.

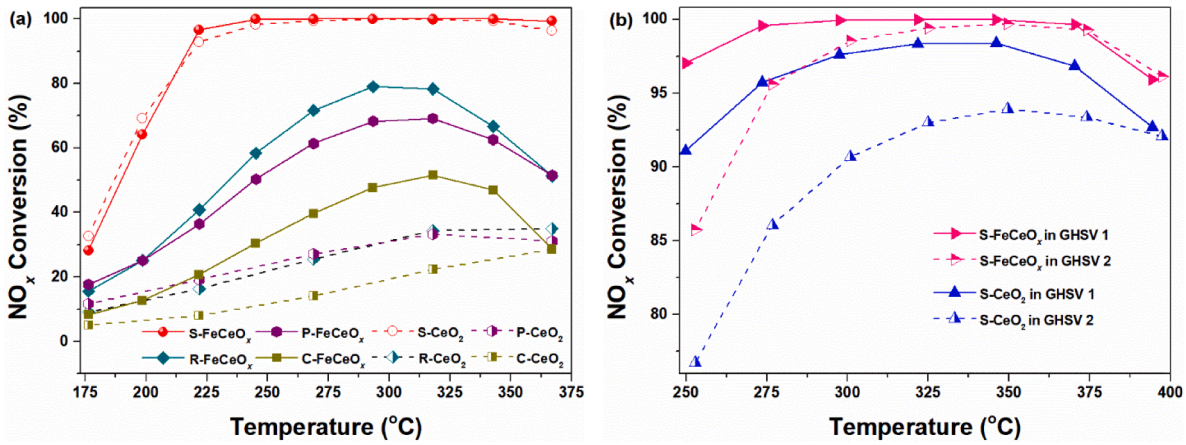

Fig. 3. NO_x conversion of prepared catalysts at different temperatures with a gaseous mixture containing 500 ppm NO_x, 500 ppm NH_3, 5 % O_2 and N_2 balance in (a) GHSV of 60, 000 mL·g^{-1}·h^{-1}, (b) GHSV 1 of 120, 000 and GHSV 2 of 240, 000 mL·g^{-1}·h^{-1}.

shown in Fig. 2 and that of R-CeO_2 and S-CeO_2 were shown in Fig. S3. CeO_2 has three low-index crystal plane group: {111}, {100} and {110}, and the interplanar spacing of (111), (200) and (220) crystal faces (shown in Fig. 1) is 0.31 nm, 0.27 nm and 0.19 nm, respectively.

As shown in Fig. 2a and e, R-$FeCeO_x$ catalyst was composed of rectangle nanorods with ca. 30–250 nm in length and 10–20 nm in width and a few nanocubes with a size range of 10–30 nm. Many lattice fringes with 0.19 nm and 0.27 nm and a few fringes with 0.31 nm were observed in nanorods. The results revealed that the nanorods of R-$FeCeO_x$ catalyst were enclosed by mostly {110}, {100} and in part {111} faces [20,21]. As depicted in Fig. S3a and 3c, R-CeO_2 catalyst was composed of nanorods with similar size and lattice fringes to that of R-$FeCeO_x$ catalyst. The growth of few nanocubes in R-$FeCeO_x$ catalyst may be induced by nitrate radical accompanying the addition of ferric nitrate in the preparation.

As shown in Fig. 2b, C-$FeCeO_x$ mainly exhibited a visible cubic morphology with a size range of 10–50 nm. As shown in Fig. 2f, a spacing of 0.27 nm assigned to (200) face was clearly observed, which confirmed that the cubes were enclosed by six {100} faces. As shown in Fig. 2c, P-$FeCeO_x$ was composed of uniform nanopolyhedra with an average size of 5–10 nm. Fig. 2g displays the HRTEM image of P-$FeCeO_x$ nanopolyhedra with interplanar spacings of 0.31 nm, 0.27 nm and 0.19 nm assigned to (111), (200) and (220) crystal faces, respectively.

As shown in Fig. 2d, S-$FeCeO_x$ was composed of uniform porous hexagon nanorods with ca. 50–100 nm in length and ca. 15 nm in width, which were more uniform and shorter than that of R-$FeCeO_x$. However, S-CeO_2 catalyst presented uniform CeO_2 nanopolyhedra with a size of ca. 10–15 nm (shown in Fig. S3b and 3d). The significant difference in morphology between S-CeO_2 and S-$FeCeO_x$ suggested that the nanorod morphology of S-$FeCeO_x$ catalyst seemed to be induced by Fe doping in the range of solid solution. The similar phenomenon was also reported in the reference [33]. The formed porous nanorod of S-$FeCeO_x$ catalyst increased its average pore diameter and pore volume. The porous structure also may increase the active sites and be conductive to a high catalytic activity and selectivity [34,35]. As shown in Fig. 2h, the lattice fringes with 0.19 nm and 0.31 nm were mostly observed and then nanorods of S-$FeCeO_x$ catalyst were also enclosed by the {110}, {100} and in part {111} faces. Some faulted lattice fringes were observed in R-$FeCeO_x$ and S-$FeCeO_x$ catalyst, indicating the existence of lattice defects in them [30].

3.2. NH_3-SCR catalytic activity

3.2.1. NO_x conversion and N_2 selectivity

As shown in Fig. 3a, the NO_x conversions of various Fe doped CeO_2 catalysts were in the following sequence: S-$FeCeO_x$ (sulfated nanorod) > R-$FeCeO_x$ (the mixture of nanorod and nanocube) > P-$FeCeO_x$ (nanopolyhedron) > C-$FeCeO_x$ (nanocube). The nanorod morphology of R-$FeCeO_x$ and S-$FeCeO_x$ catalyst with preferentially exposed {110} faces was beneficial to the NH_3-SCR reaction. S-$FeCeO_x$ had the highest NO_x

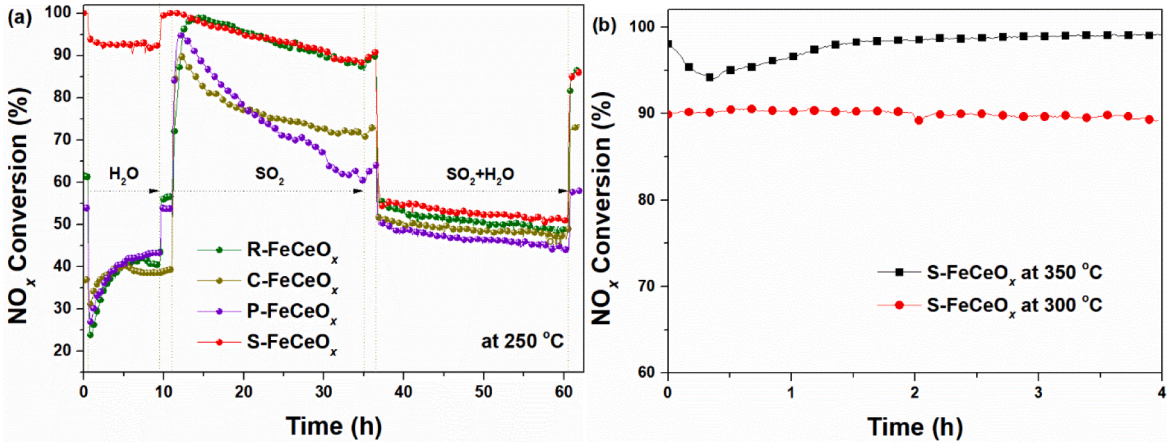

Fig. 4. The effect of H_2O, SO_2, H_2O and SO_2 on NO_x conversion of (a) R-$FeCeO_x$, C-$FeCeO_x$, P-$FeCeO_x$ and S-$FeCeO_x$ with time at 250 °C in the reaction gas containing 500 ppm NO_x, 500 ppm NH_3, 5 vol% O_2, 50 ppm SO_2 (when used), 5 vol% H_2O (when used) (b) S-$FeCeO_x$ at 300 °C and 350 °C in the reaction gas containing 500 ppm NO_x, 500 ppm NH_3, 5 vol% O_2, 200 ppm SO_2, 5 vol% H_2O with N_2 balance in GHSV of 60, 000 mL·g^{-1}·h^{-1}.

Table 2
NO_x conversions (%) of R-$FeCeO_x$, C-$FeCeO_x$, P-$FeCeO_x$ and S-$FeCeO_x$ catalysts in the test of resistance to H_2O and SO_2.

Sample	Off H_2O and SO_2	On H_2O for 9 h	Off H_2O for 1.5 h	On SO_2 for 24 h	Off SO_2 for 1.5 h	On H_2O and SO_2 for 24 h	Off H_2O and SO_2 for 1.5 h
R-$FeCeO_x$	61.3	40.5	56.5	86.5	89.8	48.4	86.8
C-$FeCeO_x$	37.1	38.6	39.3	70.2	73.1	48.0	73.2
P-$FeCeO_x$	54.0	43.3	53.9	60.1	64.0	44.0	58.1
S-$FeCeO_x$	100	92.4	100	88.1	90.7	51.4	85.8

conversion among them, which indicated sulfation and the porous nanorod morphology of S-$FeCeO_x$ catalyst may both improve its catalytic activity. The NO_x conversions of CeO_2 catalysts had similar sequence to that of $FeCeO_x$ catalysts except that NO_x conversion of R-CeO_2 was near to that of P-CeO_2. In gas hourly space velocity (GHSV) of 60, 000 $mL{\cdot}g^{-1}{\cdot}h^{-1}$, NO_x conversions of R-$FeCeO_x$, P-$FeCeO_x$ and C-$FeCeO_x$ were much higher to different degrees than that of the corresponding R-CeO_2, P-CeO_2 and C-CeO_2 at 220–375 °C, respectively, whereas NO_x conversion of S-$FeCeO_x$ was slightly higher than that of S-CeO_2 catalyst. In order to identify the difference between S-$FeCeO_x$ and S-CeO_2, their NO_x conversions were further tested in the higher GHSVs. As shown in Fig. 3b, NO_x conversions of S-$FeCeO_x$ catalyst kept above 95 % in both GHSVs of 120, 000 and 240, 000 $mL{\cdot}g^{-1}{\cdot}h^{-1}$ at 275–400 °C, which were much higher than that of S-CeO_2 catalyst. So, Fe doping considerably increased in varying degrees the NO_x conversions of these synthesized CeO_2 catalysts with different shapes at 220–375 °C.

As shown in Fig. S4a, four Fe doped CeO_2 catalysts had similar N_2 selectivity below 275 °C, and at temperatures above 275 °C, the sequence of N_2 selectivity was: S-$FeCeO_x$ > R-$FeCeO_x$ ≈ P-$FeCeO_x$ > C-$FeCeO_x$ and S-CeO_2 > C-CeO_2 > P-CeO_2 > R-CeO_2. Their N_2 selectivity decreased and the difference among them increased with temperature. R-$FeCeO_x$, P-$FeCeO_x$ and C-$FeCeO_x$ had the higher N_2 selectivity than R-CeO_2, P-CeO_2 and C-CeO_2 respectively, which indicated Fe doping improved their N_2 selectivity at 175–300 °C. As shown in Fig. S4b, no NO_2 production was observed on S-$FeCeO_x$ catalyst. NO_2 production of other catalysts increased with temperature. S-$FeCeO_x$ catalyst had the highest N_2 selectivity nearly 100 % and no N_2O and NO_2 production at whole testing temperatures 175–375 °C. It indicated that sulfation inhibited the formation of N_2O and NO_2 production.

3.2.2. *Effect of H_2O, SO_2 and their coexistence on SCR catalytic activity*

The effects of H_2O, SO_2 and their coexistence on SCR catalytic activity of R-$FeCeO_x$, C-$FeCeO_x$, P-$FeCeO_x$ and S-$FeCeO_x$ catalyst was investigated at 250 °C and the results are shown in Fig. 4(a) and summarized in Table 2. The NO_x conversions of four catalysts decreased in various degrees after introducing H_2O (q) for 9 h and then recovered to the initial values in 1.5 h without H_2O. Except S-$FeCeO_x$, R-$FeCeO_x$, C-$FeCeO_x$ and P-$FeCeO_x$ had similarly low NO_x conversions with H_2O. After introducing SO_2 into the feed gas for 1 ~ 3 h, the NO_x conversions of R-$FeCeO_x$, C-$FeCeO_x$ and P-$FeCeO_x$ catalyst sharply increased to 98.9 %, 90.0 % and 94.7 %, but that of S-$FeCeO_x$ kept stable. Based on the reported researches [24,38], the increased NO_x conversions of R-$FeCeO_x$, C-$FeCeO_x$ and P-$FeCeO_x$ catalyst after SO_2 on was because they were sulfated in flowing SO_2 at 250 °C. And then the newly formed sulfate species on them improved their surface acidity, which increased NH_3 adsorption and promoted the SCR reaction. However, NO_x conversions of S-$FeCeO_x$, R-$FeCeO_x$, C-$FeCeO_x$ and P-$FeCeO_x$ decreased to 88.1 %, 86.5 %, 70.2 % and 60.1 % respectively after inletting SO_2 for 24 h and did not recover after removing SO_2 for 1.5 h. It demonstrated they were finally poisoned by SO_2 to different degrees, which were affected obviously by their morphologies. Moreover, the simultaneous sulfation of S-$FeCeO_x$ in the synthesis process weakened the degree of SO_2 poisoning.

The sample continued to be tested in the presence of both SO_2 and H_2O. The NO_x conversions of four catalysts decreased to 51.4 %, 48.4 %, 48.0 % and 44.0 % after introducing SO_2 and H_2O for 24 h and nearly recovered after they were removed for 1.5 h. Therefore, the decrease of their NO_x conversions in the presence of H_2O and SO_2 may be due to not poison but mainly the competition adsorption between H_2O/SO_2 and NH_3/NO_x [36]. S-$FeCeO_x$ catalyst was slightly poisoned after introducing SO_2 into feeding gas and not further poisoned in the following test of resistance to both SO_2 and H_2O. The NO_x conversions of catalysts after adding SO_2 and H_2O-SO_2 for 24 h followed the sequence: S-$FeCeO_x$ > R-$FeCeO_x$ > C-$FeCeO_x$ > P-$FeCeO_x$. The above results indicated that the nanorod morphology contributed to the resistance to SO_2 and H_2O and the sulfation conducted in the synthesis process of S-$FeCeO_x$ showed a better effect than the sulfation conducted in the SO_2 resistance test of R-$FeCeO_x$. As shown in Fig. 4(b), NO_x conversions of S-$FeCeO_x$ at 300 °C and 350 °C with 200 ppm SO_2 and 5 vol% H_2O kept 89.2 % and 99.2 %, which indicated that S-$FeCeO_x$ catalyst possessed good resistance to SO_2 and H_2O above 300 °C.

Table 3
BET specific surface area, pore volume and average pore diameter of the prepared catalysts.

Sample	S_{BET} (m^2/g)	V_P (cm^3/g)	D_A (nm)
R-$FeCeO_x$	57.6	0.30	20.5
C-$FeCeO_x$	39.0	0.17	17.3
P-$FeCeO_x$	81.4	0.18	8.83
S-$FeCeO_x$	54.1	0.26	19.3
R-CeO_2	58.6	0.28	18.9
C-CeO_2	17.8	0.13	29.5
P-CeO_2	66.9	0.13	7.71
S-CeO_2	68.7	0.20	11.6

To find the reasons for the decreased deNO_x performances of the catalysts in presence of H_2O and SO_2, the XRD patterns (Fig. S5), the atomic ratios (Table S1) and the BET specific surface area (S_{BET}), pore volume (V_P) and average pore diameter (D_A) (Table S2) of used $FeCeO_x$ catalysts were determined after the test of resistance to SO_2 and H_2O. The XRD pattens of used $FeCeO_x$ catalysts nearly did not change. The determined atomic ratio of S/(Fe + Ce) in UR-$FeCeO_x$, UC-$FeCeO_x$, UP-$FeCeO_x$ and US-$FeCeO_x$ (representing used samples) was 0.061, 0.035, 0.086 and 0.068. This indicated S was deposited on the used sample in different degrees. Since the atomic ratio of S/(Fe + Ce) in S-$FeCeO_x$ was 0.046, the increase of S (0.022) on US-$FeCeO_x$ was the least during resistance test. The S_{BET} and V_P of four samples decreased due to S deposition and US-$FeCeO_x$ had the highest S_{BET}. It was reported the surface sulfates enhanced the activity of CeO_2 by improving its acidity, while the bulk sulfates resulting from the deepened sulfation process damaged its activity [37]. So, there may be two reasons for the decreased activity by inletting SO_2: the excessive sulfation of Fe doped CeO_2 catalysts and the deposition of ammonium sulfates [36,38].

To promote the application of cerium based catalysts, improving the resistance to SO_2 and H_2O is still the main direction of research. There are some strategies to weaken the poisonous effect of SO_2 and H_2O, such as the rational design of morphology and structure, metal modification, proper promoter or support, and the combination of these strategies [6,7,39]. Fe and Ce are active elements and then the acidified support with high BET specific area may improve the resistance to H_2O and SO_2 of Fe doped CeO_2 catalysts in the further study.

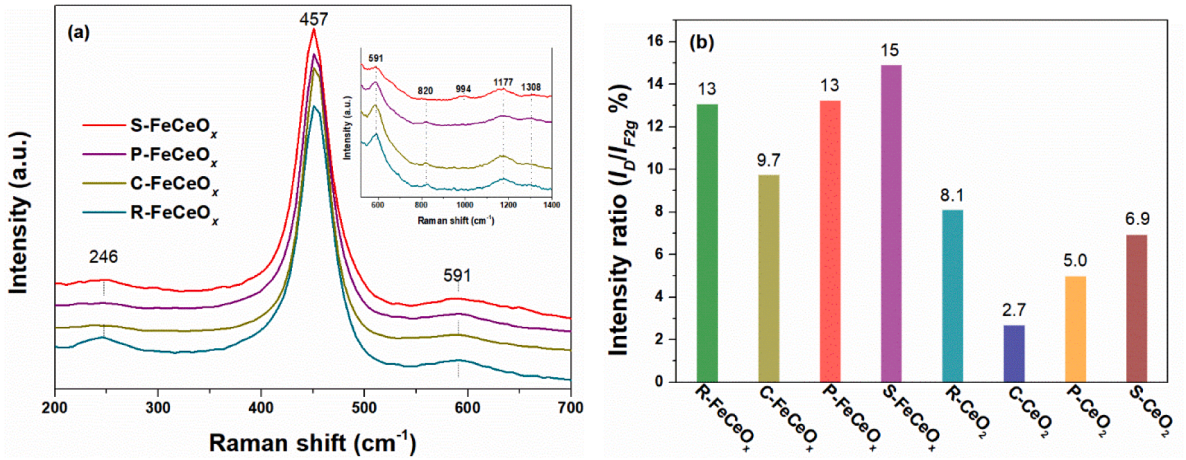

Fig. 5. (a) Raman spectra and (b) the peak intensity ratio of ID/IF$_{2g}$ in the prepared catalysts.

3.3. Physicochemical properties

3.3.1. Physical adsorption capacity

S_{BET}, V_P and D_A of the samples are shown in Table 3. The prepared CeO_2 catalysts except C-CeO_2 had similar S_{BET} but different V_P and D_A. For Fe doped CeO_2 catalysts, the sequence of S_{BET} was: P-$FeCeO_x$ > R-$FeCeO_x$ > S-$FeCeO_x$ > C-$FeCeO_x$. Fe doping improved distinctly V_P of all prepared CeO_2 catalysts and increased S_{BET} of C-CeO_2 and P-CeO_2 catalysts, which contributed to their SCR catalytic activity to some extent. Fe doping changed slightly S_{BET} and D_A of R-CeO_2 catalyst, whereas it decreased S_{BET} of S-CeO_2 catalyst. Therefore, the change of physical adsorption capacity may be not the main reason for improved SCR catalytic activity of R-$FeCeO_x$ and S-$FeCeO_x$ catalysts.

3.3.2. Raman spectra

The Raman spectra in the range of 200–700 cm^{-1} were normalized to the same height of the band at 457 cm^{-1} for the purpose of comparison. As shown in Fig. 5a, the visible Raman spectra of $FeCeO_x$ catalysts were dominated by the strong F_{2g} mode of CeO_2 at 457 cm^{-1} with weak bands at 246 cm^{-1}, 591 cm^{-1}, and 1177 cm^{-1}, corresponding to second-order transverse acoustic (2TA) mode, defect-induced (D) mode, and second-order longitudinal optical (2LO) mode, respectively. The band at 820 cm^{-1} was attributed to O−O stretching of peroxide species (O_2^{2-}) adsorbed on isolated two-electron defect sites [40]. The band at 1308 cm^{-1} was corresponding to a two magnon scattering from antiferromagnetic structure of α-Fe_2O_3 [41,42]. The band at 994 cm^{-1} only observed on S-$FeCeO_x$ catalyst was attributed to the SO symmetric stretching vibrations of SO_4^{2-} species [43].

The peak intensity at 591 cm^{-1} of defect-induced mode depends on the existence of some defects and especially is increased by oxygen vacancies formed in the ceria lattice, which contributes to the activity of the material in the SCR reaction. The relative concentrations of defect sites on these catalysts can be represented by the ratio of the peak intensity at 591 cm^{-1} to that at 457 cm^{-1} (denoted as ID/IF$_{2g}$) [10,44]. As shown in Fig. 5b, the order of these catalysts (D/F$_{2g}$) was as follows: S-$FeCeO_x$ (15 %) > R-$FeCeO_x$ (13 %) ≈ P-$FeCeO_x$ (13 %) > C-$FeCeO_x$ (9.7 %) > R-CeO_2 (8.1 %) > S-CeO_2 (6.9 %) > P-CeO_2 (5.0 %) > C-CeO_2 (2.7 %). For the prepared CeO_2 catalysts, R-CeO_2 with a nanorod shape had the most defect sites, which was in accordance with the reported results. D/F$_{2g}$ value of S-CeO_2 with a nanopolyhedron shape was higher than that of P-CeO_2 with a similar shape, which indicated that sulfation may increase the defected sites. Oxygen vacancies were increased by Fe doping to different degrees. The difference between R-$FeCeO_x$ and C-$FeCeO_x$ was less than that between R-CeO_2 and C-CeO_2, which may because Fe doping changed C-CeO_2 to a larger degree than R-CeO_2. The result agreed with that of XRD and BET. S-$FeCeO_x$ catalyst with the porous nanorods had the highest D/F$_{2g}$ value and then may have the most defect sites from oxygen vacancies induced by Fe doping and sulfation.

3.3.3. Redox property

The NH_3-SCR reaction requires a redox cycle of active sites to activate efficiently the reactants on the surface of catalysts. Weak redox ability leads to low NO_x conversion, while too strong redox ability may result in the oxidation of NO to NO_2 and unselective oxidation of NH_3 inducing poor N_2 selectivity [11,45]. H_2-TPR is used widely to examine

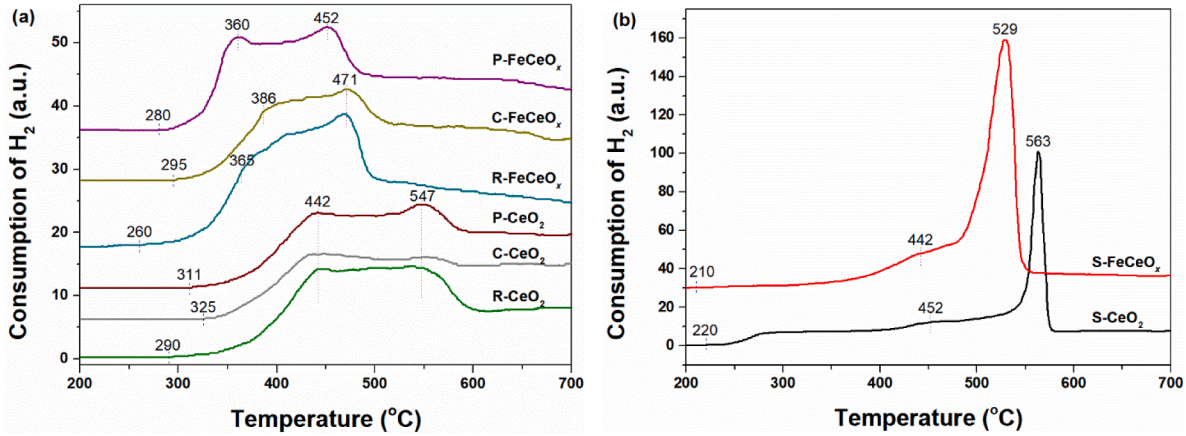

Fig. 6. H_2-TPR profiles of the prepared catalysts.

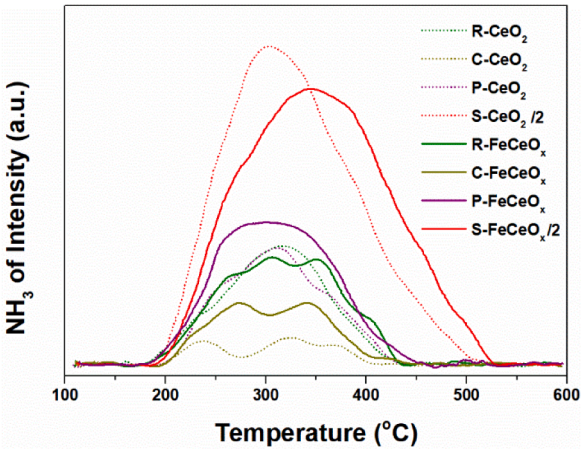

Fig. 7. NH_3-TPD-MS profiles of prepared catalysts.

redox properties of SCR catalysts. The H_2-TPR profiles of these prepared samples are presented in Fig. 6 and that without stacking lines by Y offsets are shown in Fig. S6 for clear comparison of peak intensity. As shown in Fig. 6a, for R-CeO_2, C-CeO_2 and P-CeO_2 samples, only a broad band was observed in the range of ca. 300–600 °C with two max values at about 442 °C and 547 °C, assigned to the reduction of surface adsorbed oxygen on oxygen vacancies and surface lattice oxygen. After Fe doping, their bands became higher and shifted to the lower temperature range of ca. 260–520 °C, demonstrating that Fe doping into CeO_2 lattice weakened Ce-O bond and enhanced oxygen vacancies in iron-cerium oxide solid solution [30,46]. The peaks at 360–386 °C were assigned to the overlap of the reduction peak of surface oxygen species adsorbed on oxygen vacancies and that of $Fe_2O_3 \rightarrow Fe_3O_4$ on Fe doped CeO_2 samples. As shown in Fig. 6b, the distinctive H_2 reduction peaks at 563 °C and 529 °C on S-CeO_2 and S-$FeCeO_x$ catalysts respectively were much higher than that of other catalysts and mainly attributed to the reduction of surface metal sulfate species [8,26], which were simultaneously synthesized in the hydrothermal preparation of S-CeO_2 and S-$FeCeO_x$ catalysts. The presence of sulfate species was also proved by XRF and Raman.

The lower onset of reduction temperature was conductive to the higher redox ability and then catalytic activity. The onset of reduction over Fe doped CeO_2 catalysts shifted to the lower temperature than that over CeO_2 catalysts, which manifested Fe doping improved their redox ability. The sequence in onset of reduction temperature for these samples was: S-$FeCeO_x$ < R-$FeCeO_x$ < P-$FeCeO_x$ < C-$FeCeO_x$, which agreed with the sequence of their NO_x conversion. The same rule was observed among CeO_2 catalysts. As shown in Fig. S6, the TPR peak area at 260–520 °C was in the following order: R-$FeCeO_x$ > P-$FeCeO_x$ > C-$FeCeO_x$. Therefore, based on the above results, their redox ability was in the sequence of R-$FeCeO_x$ > P-$FeCeO_x$ > C-$FeCeO_x$, which was consistent with the sequence of their NO_x conversion. At 260–400 °C, the TPR peak area of S-$FeCeO_x$ was smallest, and its redox ability was inhibited by surface metal sulfate species in comparison to other $FeCeO_x$ catalysts [36]. Hence, that may be one of the reasons for the highest N_2 selectivity due to the suppressed catalytic oxidization of NH_3 to N_2O and the lowest oxidation of NO to NO_2 on S-$FeCeO_x$ catalyst (shown in Fig. S4). To sum up, the redox properties of these prepared catalysts was affected variously by Fe doping, morphology and sulfate.

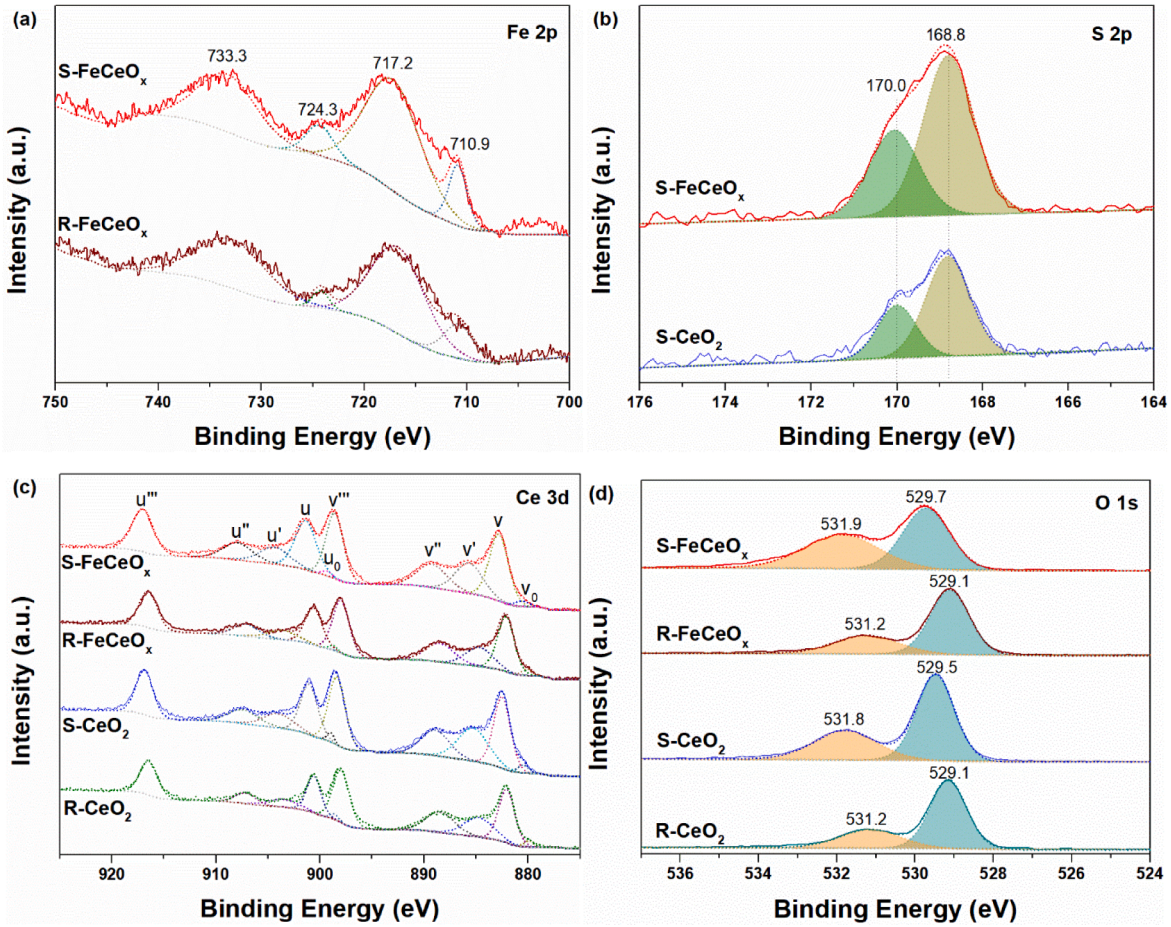

Fig. 8. (a) Fe 2p, (b) S 2p, (c) Ce 3d, (d) O 1 s XPS spectra of S-$FeCeO_x$, R-$FeCeO_x$, S-CeO_2 and R-CeO_2 catalysts.

Table 4
Surface atomic ratios (%) from XPS over samples.

Sample	$Ce^{3+}/(Ce^{3+}+Ce^{4+})$	$O_\beta/(O_\alpha + O_\beta)$
R-$FeCeO_x$	18.37	31.22
S-$FeCeO_x$	20.76	46.64
R-CeO_2	19.68	30.75
S-CeO_2	23.43	35.86

3.3.4. Surface acidity

The adsorption and activation of NH_3 is the key step of NH_3-SCR reaction, which greatly depends on surface acidity of SCR catalyst. The amount and strength of surface acid sites on the prepared catalysts were investigated by NH_3-TPD test and the results were shown in Fig. 7. The bands below 200 °C, in the range of 200–350 °C and above 350 °C are generally ascribed to the NH_3 desorption on weak, medium and strong acid sites, respectively [47]. The peak area of NH_3 desorption on each $FeCeO_x$ catalyst was larger than that of the corresponding CeO_2 catalyst. The results showed that Fe doping increased acid sites of these CeO_2 catalysts to different degree. The NH_3 desorption peak of R-$FeCeO_x$ catalyst was larger than that of R-CeO_2 catalyst mainly at temperatures above 350 °C, which demonstrated that Fe doping mainly increased its strong acid sites. The peak area of NH_3 desorption on Fe doped CeO_2 catalysts was in the following order: S-$FeCeO_x$ > P-$FeCeO_x$ > R-$FeCeO_x$ > C-$FeCeO_x$ and the similar order was observed among CeO_2 catalysts except that the peak area of R-CeO_2 was similar to that of P-CeO_2 catalyst. Because the same precipitant was used in the preparation, the difference between the surface acidity of R-$FeCeO_x$ and C-$FeCeO_x$ was affected by their shapes. R-$FeCeO_x$ with a nanorod shape had the higher surface acidity than C-$FeCeO_x$ with a nanocube shape. Compared with R-$FeCeO_x$, P-$FeCeO_x$ had the higher surface acidity due to using ammonia as its precipitant. The presented signal of NH_3 desorption on S-$FeCeO_x$ was a half of the real signal. Then, S-$FeCeO_x$ had far more acid sites than other $FeCeO_x$ catalysts, which resulted from surface metal sulfate species and could further improve the NH_3-SCR activity.

3.3.5. XPS analysis

S-$FeCeO_x$ and R-$FeCeO_x$ catalysts were concerned, because both of them presented nanorod shape and their NO_x conversion ranked the first and the second among Fe doped CeO_2 catalysts. Fig. 8 shows Fe 2p, S 2p, Ce 3d and O 1 s XPS spectra of S-$FeCeO_x$, R-$FeCeO_x$, S-CeO_2 and R-CeO_2 catalysts. Two peaks at 724.3 eV and 710.9 eV and satellite peaks (near 733.3 eV and 717.2 eV) were clearly observed on Fe 2p spectra of S-$FeCeO_x$ and R-$FeCeO_x$ catalyst (Fig. 8a), which could be assigned to $2p_{1/2}$ and $2p_{3/2}$ of Fe^{3+} [30,48]. The presence of SO_4^{2-} on S-$FeCeO_x$ and S-CeO_2 was also supported by the XPS spectra over S 2p region. As shown in Fig. 8b, The S 2p peaks mainly centering at 170.0 eV and 168.8 eV could be assigned to S $2p_{1/2}$ and $2p_{3/2}$ of metal sulfate species [49].

Ce 3d spectrum is composed of two multiplets (u and v), which are assigned to two spin orbit peaks $3d_{3/2}$ and $3d_{5/2}$, respectively. As shown in Fig. 8c, the Ce 3d XPS spectrum of each catalyst was deconvoluted into ten peaks. The peaks labeled u''', v''', u'', v'', u and v were associated with Ce^{4+}. The peaks labeled u_0, v_0, u' and v' were assigned to Ce^{3+} [50,51]. The binding energy of peak position is listed in Table S3. As shown in Table 4, R-$FeCeO_x$ and S-$FeCeO_x$ catalysts had lower $Ce^{3+}/(Ce^{3+}+Ce^{4+})$ ratios than R-CeO_2 and S-CeO_2, which indicated Fe doping decreased their $Ce^{3+}/(Ce^{3+}+Ce^{4+})$ ratios. Oxygen vacancies conductive to SCR reaction were generated in two pathways. On one hand, intrinsic oxygen vacancies will form to maintain electrostatic balance as soon as Ce^{3+} exists in fluorite CeO_2 [19]. The higher Ce^{3+} proportion could generate more oxygen vacancies. On the other hand, the doping of Fe^{3+} into CeO_2 lattice formed the extrinsic oxygen vacancies [31]. Therefore, for S-$FeCeO_x$ and R-$FeCeO_x$, although the introduction of Fe^{3+} into CeO_2 decreased their Ce^{3+} ratios and then the intrinsic oxygen vacancies, it generated more extrinsic oxygen vacancies based on the results of XRD and Raman. S-$FeCeO_x$ catalyst had the higher $Ce^{3+}/(Ce^{3+}+Ce^{4+})$ ratio than R-$FeCeO_x$, which manifested the introduction of S increased Ce^{3+} ratio. Ce^{4+} in S-$FeCeO_x$ catalyst could be reduced to Ce^{3+} by forming the metal sulfate [36,52].

The O 1 s spectra of samples (Fig. 8d) have been resolved into two peaks assigned to the lattice oxygen (O_α) of the metal oxides at 529.1–529.7 eV and surface chemisorbed oxygen (O_β) on oxygen vacancies and −OH groups at 531.2–531.9 eV, respectively [53]. The binding energy of O 1 s peaks in S-$FeCeO_x$ catalyst was somewhat higher than that in R-$FeCeO_x$ catalysts, which indicated the electron redistribution between Fe, Ce cations and surface sulfate species [36]. As listed in Table 4, Fe doping increased the ratio of $O_\beta/(O_\alpha + O_\beta)$, and moreover the coexistence of Fe and S enhanced it largely. S-$FeCeO_x$ catalyst showed the highest ratio of surface chemisorbed oxygen which is more active due to its better mobility than lattice oxygen. Then, it also might possess the most oxygen vacancies and hydroxyl groups as Brønsted acid sites, which improved NH_3 adsorption and activation and then supplied abundant reductant on S-$FeCeO_x$ catalyst surface for SCR of NO_x [45].

3.4. NH_3-SCR reaction mechanism

3.4.1. DRIFTS study

DRIFTS is a useful tool to investigate the nature of adsorbed reactants on the surface of catalyst. As shown in Fig. 9a, the characteristics of infrared bands of NH_3 adsorbed species over the samples were observed after 500 ppm NH_3 adsorption in N_2 balance for 30 min and high pure N_2

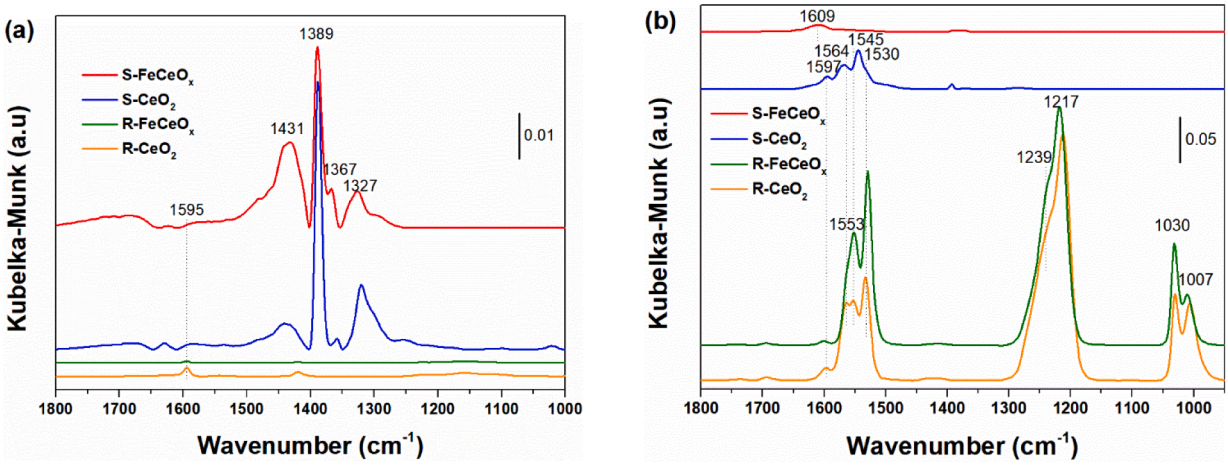

Fig. 9. DRIFTS of R-$FeCeO_x$, R-CeO_2, S-$FeCeO_x$ and S-CeO_2 catalysts exposed to (a) 500 ppm NH_3/N_2 and (b) 500 ppm NO + 5 % O_2/N_2 for 30 min followed with 20 min N_2 purge at 250 °C.

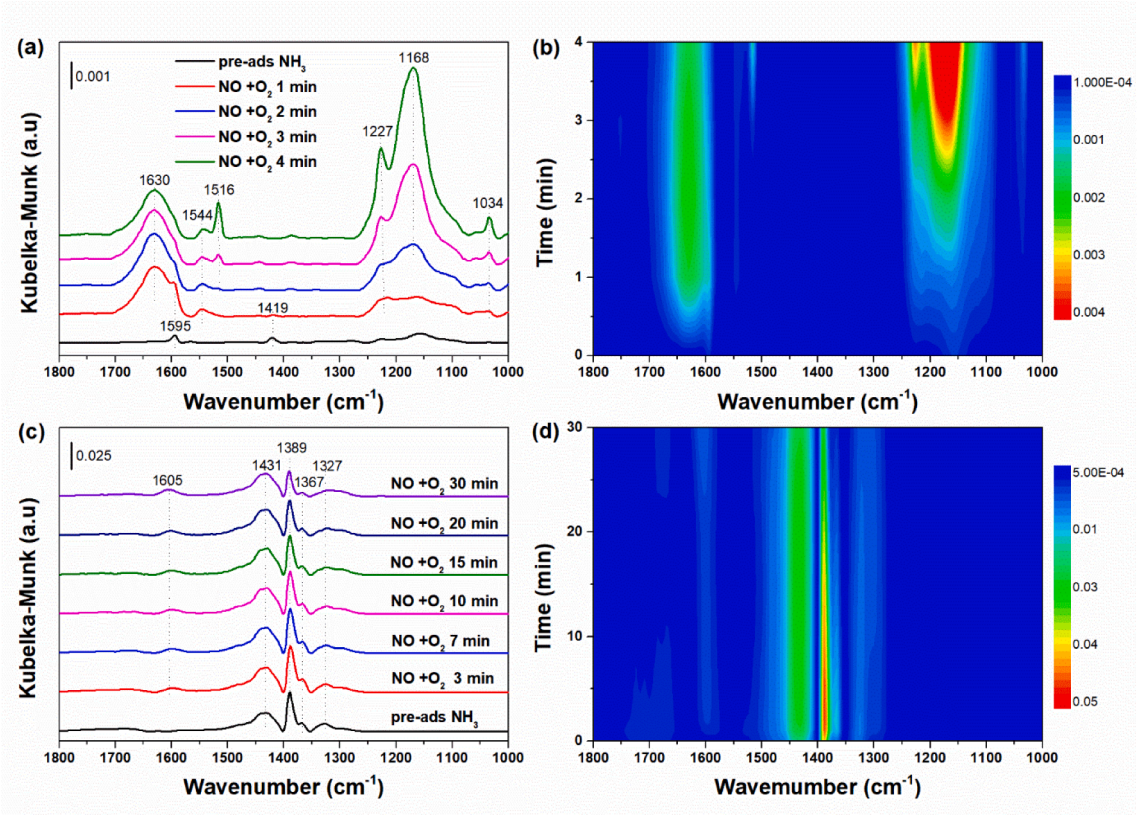

Fig. 10. In situ DRIFTs spectra of NO + O_2 reacting with pre-adsorbed NH_3 species over (a) R-FeCeO$_x$, (c) S-FeCeO$_x$, and the corresponding mapping results over (b) R-FeCeO$_x$, (d) S-FeCeO$_x$ catalyst at 250 °C.

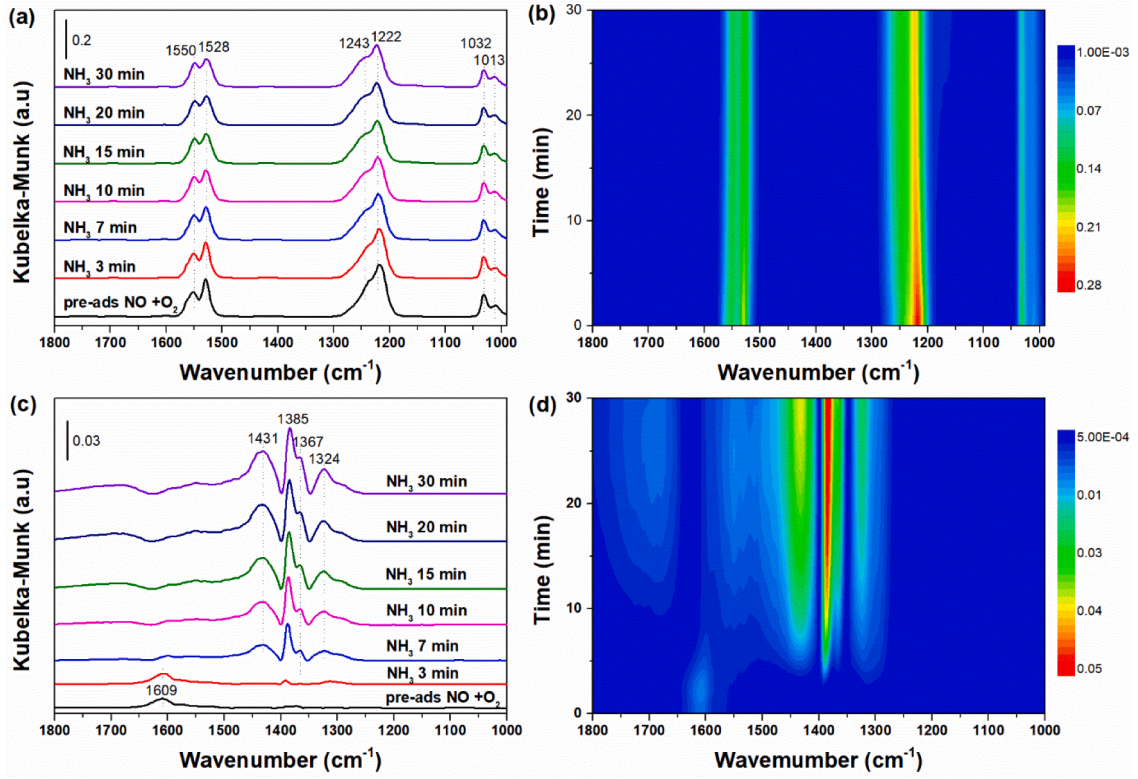

Fig. 11. In situ DRIFTs spectra of NH_3 reacted with pre-adsorbed NO + O_2 species over (a) R-FeCeO$_x$, (c) S-FeCeO$_x$, and the corresponding mapping results over (b) R-FeCeO$_x$, (d) S-FeCeO$_x$ catalyst at 250 °C.

purge for 20 min. The bands at 1595 and 1419 cm^{-1} were observed on R-$FeCeO_x$ and R-CeO_2 catalysts. The bands at 1800–1610, 1595, 1431, 1389, 1367 and 1327 cm^{-1} were observed on S-$FeCeO_x$ and S-CeO_2 catalysts. The bands at 1595 cm^{-1} were assigned to asymmetric bending vibration of coordinated NH_3 on Lewis acid sites. The bands from 1800 to 1610 cm^{-1} and bands at 1431 cm^{-1} and 1419 cm^{-1} were attributed to the symmetric and asymmetric deformation mode of NH_4^+ on Brønsted acid sites [54,55]. The bands at 1389 cm^{-1} were assigned to asymmetric deformation mode of NH_4^+ on surface sulfates. The bands at 1367 and 1327 cm^{-1} belonged to the wagging mode of $–NH_2$ species. The adsorbed NH_3 would be oxidized to adsorbed $–NH_2$ species by the activated oxygen on surface active sites [2,24,56]. The NH_3 adsorption peaks observed on S-$FeCeO_x$ and S-CeO_2 catalysts were much stronger than that on R-$FeCeO_x$ and R-CeO_2 catalysts. Many Brønsted acid sites and a few Lewis acid sites formed and the adsorption of NH_3 was enhanced in the presence of metal sulfate species. According to reported researches, surface metal sulfates interacted with water and then generated Brønsted acid sites on S-$FeCeO_x$ catalyst [8,57].

As seen from Fig. 9b, after 500 ppm NO and 5 % O_2 adsorption in N_2 balance for 30 min and high pure N_2 purge for 20 min, the infrared bands attributed to monodentate nitrate (1530, 1239 and 1007 cm^{-1}), bidentate nitrate (1564, 1553, 1545 and 1030 cm^{-1}), bridging nitrate (1609, 1597 and 1217 cm^{-1}) were observed [45,58]. Fe doping weakened the NO_x adsorption on S-$FeCeO_x$ and R-$FeCeO_x$ catalysts. The NO_x adsorption peaks observed on S-$FeCeO_x$ and S-CeO_2 catalysts were much weaker than that on R-$FeCeO_x$ and R-CeO_2 catalysts. It demonstrated that the adsorption of NO_x was restrained in the presence of metal sulfate species, probably because the enhanced surface acidity was adverse to the adsorption of acidic substance. Based on the comparison between Fig. 9a and b, S-$FeCeO_x$ catalyst presented totally different adsorption behavior from R-$FeCeO_x$ catalyst. The strong NO_x adsorption and weak NH_3 adsorption were observed on R-$FeCeO_x$ catalyst. However, the strong NH_3 adsorption and weak NO_x adsorption were observed on S-$FeCeO_x$ catalyst, which mainly be due to the introduction of SO_4^{2-}.

To explore the NH_3-SCR reaction mechanism over R-$FeCeO_x$ and S-$FeCeO_x$ catalyst, the transient reaction between NO + O_2 and NH_3 was investigated and the results collected by *in situ* DRIFTS were shown in Fig. 10 and Fig. 11. As comparison, the results of R-CeO_2 and S-CeO_2 catalysts were shown in Fig. S7 and Fig. S8. These catalysts firstly adsorbed 500 ppm NH_3 in N_2 balance for 30 min and then were purged with high pure N_2 for 20 min. Finally, 500 ppm NO and 5 % O_2 in N_2 balance was introduced into the reaction chamber, and the spectra were recorded every minute at 250 °C. As shown in Fig. 10a and b, the weak bands at 1595 cm^{-1} (Lewis acid sites) and 1419 cm^{-1} (Brønsted acid sites) of adsorbed NH_3 species on R-$FeCeO_x$ catalyst gradually decreased with time and disappeared after the introduction of NO + O_2 for 4 min due to the consumption of NH_3 species. On the other hand, the strong bands attributed to NO_x appeared after the introduction of NO + O_2 and then increased with time. As shown in Fig. S7a and b, R-CeO_2 catalyst had similar reaction process to R-$FeCeO_x$ catalyst. This indicated the possible presence of weak SCR reaction following Eley-Rideal (E-R) mechanism on R-CeO_2 and R-$FeCeO_x$ catalyst, in which the adsorbed NH_3 species on acid sites react with gaseous NO and O_2 into N_2 and H_2O [59].

As shown in Fig. 10c and d, the bands at 1431, 1389 (Brønsted acid sites) and 1367 cm^{-1}, 1327 cm^{-1} ($–NH_2$) of adsorbed NH_3 species on S-$FeCeO_x$ catalyst gradually decreased with time after the introduction of NO + O_2, which was due to the reaction between NO + O_2 and pre-adsorbed NH_3 species. Then, the gas phase NO could bond with $–NH_2$ and form an important intermediate $–NH_2NO$, which could then decompose into N_2 and H_2O. Notably, the consumption of the band at 1389 cm^{-1} assigned to asymmetric deformation mode of NH_4^+ on surface sulfates was faster than other adsorbed NH_3 species, indicating it was more active. On the other hand, the weak band at 1605 cm^{-1} attributed to bridging nitrate appeared after the introduction of NO + O_2 for 3 min and then increased with time, which also indicated NO_x were weakly adsorbed on S-$FeCeO_x$ catalyst. As shown in Fig. S7c and d, S-CeO_2 catalyst had similar reaction process to S-$FeCeO_x$ catalyst. This manifested the presence of E-R reaction mechanism on S-CeO_2 and S-$FeCeO_x$ catalyst.

To further explore their reaction mechanism, the experiment process in the reversed order was investigated and the results are shown in Fig. 11. That is, the catalyst firstly was pre-adsorbed with 500 ppm NO and 5 % O_2 in N_2 balance for 30 min followed with N_2 purge for 20 min and then was exposed to 500 ppm NH_3 in N_2 balance at 250 °C. As shown in Fig. 11a and b, the bands attributed to monodentate nitrate (1528, 1243 and 1013 cm^{-1}), bidentate nitrate (1550 and 1032 cm^{-1}), bridging nitrate (1222 cm^{-1}) on R-$FeCeO_x$ decreased gradually with time after introducing NH_3. Notably, the bands at 1528 cm^{-1} and 1222 cm^{-1} assigned to monodentate and bridging nitrate decreased faster than other adsorbed NO_x species, implying they were more active. As shown in Fig. S8a and b, R-CeO_2 had similar reaction process to R-$FeCeO_x$. This manifested the presence of Langmuir-Hinshelwood (L-H) mechanism on R-CeO_2 and R-$FeCeO_x$ catalyst, in which adsorbed NO_x could react with adsorbed NH_3 [60]. As shown in Fig. 11c and d, the weak band at 1609 cm^{-1} assigned to bridging nitrate on S-$FeCeO_x$ catalyst decreased gradually and disappeared after the introduction of NH_3 for 7 min. Meanwhile, several strong bands of adsorbed NH_3 species (1431, 1385, 1367, and 1324 cm^{-1}) formed and increased with time. As shown in Fig. S8c and d, S-CeO_2 had similar reaction process, in which the weak band at 1595 cm^{-1} disappeared. This indicated the possible existence of L-H mechanism on S-CeO_2 and S-$FeCeO_x$ catalyst. Based on the above results, the NH_3-SCR reaction on R-CeO_2 and R-$FeCeO_x$ catalyst mainly followed L-H mechanism, while the NH_3-SCR reaction on S-CeO_2 and S-$FeCeO_x$ catalyst mainly followed E-R mechanism. Fe doping into S-CeO_2 and R-CeO_2 catalyst did not change their NH_3-SCR reaction mechanism. Sulfates in S-$FeCeO_x$ catalyst made its reaction mechanism different from that of R-$FeCeO_x$ catalyst, which may because they changed significantly the adsorption behavior of NH_3 and NO_x on S-$FeCeO_x$ catalyst [8,26].

3.4.2. NH_3-SCR reaction mechanism

The main structure of R-$FeCeO_x$, C-$FeCeO_x$, P-$FeCeO_x$ and S-$FeCeO_x$ was iron-cerium oxide solid solution with different exposed crystal faces and defect sites. Besides, surface metal sulfates formed on S-$FeCeO_x$ catalyst and also participated in SCR rection. In the synthesis of S-$FeCeO_x$ catalyst, Na_2S hydrolysis gives rise to OH^- ions and H_2S. Then, OH^- reacted with hydrate Ce^{3+}, Fe^{3+} ions and O_2 to form Fe doped CeO_2 and meanwhile H_2S reacted with a part of precursors and O_2 to form surface metal sulfates maybe including cerous sulfate $Ce_2(SO_4)_3$, ceric sulfate $Ce(SO_4)_2$ and ferric sulfate $Fe_2(SO_4)_3$ [25,29]. TPR and XPS proved the interaction between Fe and Ce and the existence of active sites including surface Ce^{4+}–Ce^{3+}, Fe^{3+}–Fe^{2+}, oxygen species and SO_4^{2-}. Essentially, the high surface acidity and suitable redox ability benefit to SCR activity. Therefore, the influence mechanisms of morphology and sulfation are attributed to their effect on redox ability and surface acidity of these catalysts. It is generally believed that the surface oxygen vacancies contribute to redox ability and then catalytic activity. The formation of oxygen vacancies by Fe doping into CeO_2 depends on the morphology. Their crystallinity is in sequence of C-$FeCeO_x$ > R-$FeCeO_x$ > P-$FeCeO_x$ > S-$FeCeO_x$. Iron-cerium oxide solid solution provides many defect sites for the adsorption and activation of ammonia and the lower crystallinity means more lattice defects such as oxygen vacancies. Moreover, oxygen vacancies are predicted to be more stable at low-index surfaces than in the bulk. The results of density functional theory calculation reveal that the catalytic activity of different exposed faces of CeO_2 follows the sequence of {110} > {100} > {111} [24,61]. The order of lattice defects and redox ability detected by Raman and TPR is as follows: R-$FeCeO_x$ > P-$FeCeO_x$ > C-$FeCeO_x$. Hence, the nanorod morphology with preferentially exposed {110} faces and more oxygen vacancies is beneficial to redox ability. S-$FeCeO_x$ may have the most defect sites from oxygen vacancies induced by Fe doping and sulfation

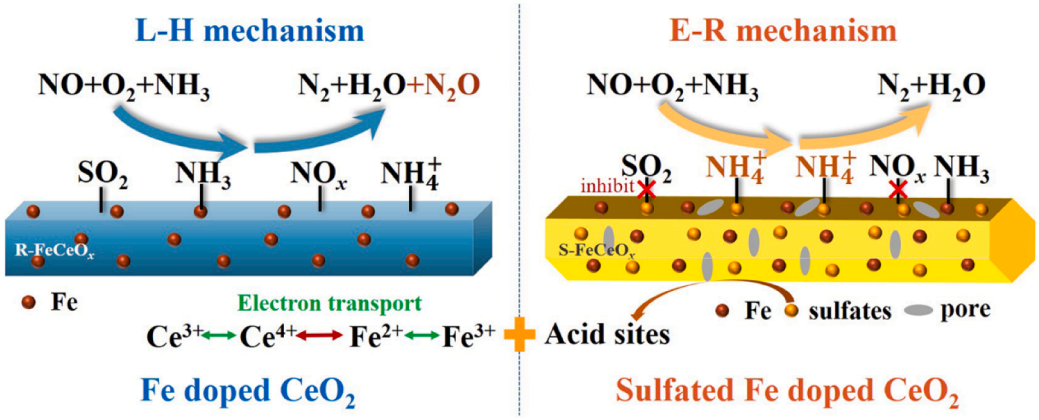

Scheme 1. Schematic diagram of NH_3-SCR reaction on R-$FeCeO_x$ and S-$FeCeO_x$ nanorod catalyst.

but its redox ability is inhibited slightly by surface metal sulfates at low temperatures. S-$FeCeO_x$ had far more acid sites from the surface metal sulfate species than other $FeCeO_x$ catalysts. The highest surface acidity and suitable redox ability benefit to the optimal SCR activity of S-$FeCeO_x$ catalyst.

The NO_x conversions of these catalysts after inletting SO_2 and H_2O-SO_2 for 24 h follow the sequence of S-$FeCeO_x$ > R-$FeCeO_x$ > C-$FeCeO_x$ > P-$FeCeO_x$. During SO_2 resistance test, R-$FeCeO_x$, C-$FeCeO_x$ and P-$FeCeO_x$ catalyst first are sulfated accompanied with improved NO_x conversions and then gradually poisoned by SO_2. This sulfation effect may depend on their morphologies and redox abilities. The highest redox ability of R-$FeCeO_x$ may facilitate the fastest sulfation on the surface and then the covering of surface sulfates may slightly prohibit the further sulfation in the bulk and the deposition of ammonium sulfates. And the weakest redox ability of C-$FeCeO_x$ may result in the slowest sulfation and deposition, and the balance between them might make it have the higher SO_2 resistance than P-$FeCeO_x$. In addition, the simultaneous sulfation of S-$FeCeO_x$ in the synthesis process weakens the degree of SO_2 poisoning. Therefore, the nanorod morphology with preferentially exposed {110} faces and more surface oxygen vacancies and the surface sulfation improved significantly the NH_3-SCR activity and SO_2 resistance.

Based on *in situ* DRIFTs results, the different NH_3-SCR reaction mechanisms on the R-$FeCeO_x$ and S-$FeCeO_x$ catalyst are proposed and shown in Scheme 1. R-$FeCeO_x$ catalyst presents the typical rectangle nanorod shape. Fe doping into CeO_2 nanorod enhances oxygen vacancies and redox ability. The NH_3-SCR reaction on R-$FeCeO_x$ catalyst mainly follows L-H mechanism, and Fe doping into CeO_2 catalysts does not change its NH_3-SCR reaction mechanism. In S-$FeCeO_x$ catalyst, the simultaneous Fe doping and sulfation induces the morphology of porous hexagon nanorod with significantly enhanced oxygen vacancies, more exposed active sites and accelerated electron transport in S-$FeCeO_x$ catalyst [62]. The NH_3-SCR reaction on S-$FeCeO_x$ catalyst mainly follows E-R mechanism and the sulfation makes it have a different reaction mechanism from R-$FeCeO_x$ catalyst. On the one hand, the surface metal sulfates generate many Brønsted acid sites to greatly enhance the adsorption of NH_3 and then NO_x conversion. On the other hand, they suppress NO_x adsorption and the side reaction of NH_3 oxidation, which effectively decreases N_2O production and then improves N_2 selectivity [36].

4. Conclusions

Fe doped CeO_2 catalysts presented distinct morphology dependent SCR catalytic activity. Their NO_x conversions were in the following sequence: S-$FeCeO_x$ (sulfated porous nanorod) > R-$FeCeO_x$ (the mixture of nanorod and nanocube) > P-$FeCeO_x$ (nanopolyhedron) > C-$FeCeO_x$ (nanocube). Fe doping enhanced significantly the NO_x conversions of these CeO_2 catalysts in varied degrees. The simultaneous Fe doping and sulfation in S-$FeCeO_x$ catalyst induced porous hexagon nanorod shape with preferentially exposed {110} faces, which presented the largest concentration of oxygen vacancies and surface chemisorbed oxygen. The surface acid sites and redox ability were changed by surface metal sulfates on S-$FeCeO_x$ catalyst, which increased considerably Brønsted acid sites for NH_3 adsorption and suppressed NO_x adsorption and the catalytic oxidization of NH_3 to N_2O. That improved NO_x conversions and N_2 selectivity on S-$FeCeO_x$ catalyst and changed its reaction mechanism. The NH_3-SCR reaction on R-$FeCeO_x$ catalyst mainly followed L-H mechanism, while that on S-$FeCeO_x$ catalyst mainly followed E-R mechanism. This work is beneficial to understanding the facet-dependent effect of Fe doped CeO_2 on the NH_3-SCR reaction, and helpful to provide a strategy for modifying the structure and surface properties to obtain efficient SCR catalysts. In the further study, the acidified support with high BET specific area may improve the resistance to H_2O and SO_2 of Fe doped CeO_2 catalysts and also promote the economic efficiency for the industrial application.

CRediT authorship contribution statement

Jinxiu Wang: Conceptualization, Investigation, Formal analysis, Writing – original draft, Funding acquisition. **Yuqiu Liu:** Investigation. **Xianfang Yi:** Investigation. **Yanting Chen:** Formal analysis. **Yanke Yu:** Writing – review & editing. **Jinsheng Chen:** Supervision, Writing – review & editing, Funding acquisition.

Declaration of Competing Interest

The authors declare that they have no known competing financial interests or personal relationships that could have appeared to influence the work reported in this paper.

Data availability

Data will be made available on request.

Acknowledgement

This work is financially supported by the Cultivating Project of Strategic Priority Research Program of Chinese Academy of Sciences [XDPB1902], Fujian Provincial Department of Science and Technology, China [2020Y0085] and Youth Innovation Promotion Association, Chinese Academy of Sciences [2020309].

Appendix A. Supplementary data

Supplementary data to this article can be found online at https://doi.org/10.1016/j.fuel.2022.126771.

References

[1] Pan Y, Shen B, Liu L, Yao Y, Gao H, Liang C, et al. Develop high efficient of NH_3-SCR catalysts with wide temperature range by ball-milled method. Fuel 2020;282:118834. https://doi.org/10.1016/j.fuel.2020.118834.

[2] Yi X, Wang J, Liu Y, Chen Y, Chen J. Promotional effect of Fe and Ce co-doping on a V_2O_5–WO_3/TiO_2 catalyst for SCR of NO_x with high K and Pb resistance. Catal Sci Technol 2022;12:4169–80. https://doi.org/10.1039/d2cy00818a.

[3] Li J, Chang H, Ma L, Hao J, Yang RT. Low-temperature selective catalytic reduction of NO_x with NH_3 over metal oxide and zeolite catalysts—A review. Catal Today 2011;175:147–56. https://doi.org/10.1016/j.cattod.2011.03.034.

[4] Fu M, Li C, Lu P, Qu L, Zhang M, Zhou Y, et al. A review on selective catalytic reduction of NO_x by supported catalysts at 100–300 °C—catalysts, mechanism, kinetics. Catal Sci Technol 2014;4:14–25. https://doi.org/10.1039/c3cy00414g.

[5] Wei LG, Guo RT, Zhou J, Qin B, Chen X, Bi ZX, et al. Chemical deactivation and resistance of Mn-based SCR catalysts for NO_x removal from stationary sources. Fuel 2022;316:123438. https://doi.org/10.1016/j.fuel.2022.123438.

[6] Cai M, Bian X, Xie F, Wu W, Cen P. Preparation and performance of cerium-based catalysts for selective catalytic reduction of nitrogen oxides: A critical review. Catalysts 2021;11:361. https://doi.org/10.3390/catal11030361.

[7] Xu J, Yu H, Zhang C, Guo F, Xie J. Development of cerium-based catalysts for selective catalytic reduction of nitrogen oxides: a review. New J Chem 2019;43:3996–4007. https://doi.org/10.1039/c8nj05420g.

[8] Ma L, Seo CY, Nahata M, Chen X, Li J, Schwank JW. Shape dependence and sulfate promotion of CeO_2 for selective catalytic reduction of NO with NH_3. Appl Catal B: Environ 2018;232:246–59. https://doi.org/10.1016/j.apcatb.2018.03.065.

[9] Wang J, Yi X, Ng D, Li H, Miao J, Su Q, et al. Synthesis and characterization of Mn–Ce–VO_x/TiO_2 nanocomposite for SCR of NO_x at low temperatures: role of Mn, Ce and V oxide. Top Catal 2020;63:913–23. https://doi.org/10.1007/s11244-020-01315-x.

[10] Wu XM, Yu XL, Huang ZW, Shen HZ, Jing GH. MnOx-decorated VOx/CeO2 catalysts with preferentially exposed 110 facets for selective catalytic reduction of NOx by NH3. Appl Catal B: Environ 2020;268:118419. https://doi.org/10.1016/j.apcatb.2019.118419.

[11] Wang J, Yi X, Su Q, Chen J, Xie Z. Effect of FeO_x and MnO_x doping into the CeO_2–V_2O_5/TiO_2 nanocomposite on the performance and mechanism in selective catalytic reduction of NO_x with NH_3. Catal Sci Technol 2021;11:2852–63. https://doi.org/10.1039/d0cy02471f.

[12] Wang F, Shen B, Zhu S, Wang Z. Promotion of Fe and Co doped Mn-Ce/TiO_2 catalysts for low temperature NH_3-SCR with SO_2 tolerance. Fuel 2019;249:54–60. https://doi.org/10.1016/j.fuel.2019.02.113.

[13] Yao X, Zhao W, Rong J, Luo W, Kang K, Long L, et al. Influence of preparation methods of supports on the deNO_x performance and alkali-metal resistance over TiO_2/CeO_2 catalysts in NH_3-SCR reaction. Fuel 2022;320:123920. https://doi.org/10.1016/j.fuel.2022.123920.

[14] Zhang XJ, Zhang TJ, Song ZX, Liu W, Xing Y. Effect of sulfate species on the performance of Ce-Fe-O_x catalysts in the selective catalytic reduction of NO by NH_3. J Fuel Chem Technol 2021;49:844–52. https://doi.org/10.1016/s1872-5813(21)60021-x.

[15] Husnain N, Wang E, Li K, Anwar MT, Mehmood A, Gul M, et al. Iron oxide-based catalysts for low-temperature selective catalytic reduction of NO_x with NH_3. Rev Chem Eng 2019;35:239–64. https://doi.org/10.1515/revce-2017-0064.

[16] Wang H, Qu Z, Xie H, Maeda N, Miao L, Wang Z. Insight into the mesoporous $Fe_xCe_{1-x}O_{2-\delta}$ catalysts for selective catalytic reduction of NO with NH_3: Regulable structure and activity. J Catal 2016;338:56–67. https://doi.org/10.1016/j.jcat.2016.02.009.

[17] Huang W, Gao Y. Morphology-dependent surface chemistry and catalysis of CeO_2 nanocrystals. Catal Sci Technol 2014;4:3772–84. https://doi.org/10.1039/c4cy00679h.

[18] Mai HX, Sun LD, Zhang YW, Si R, Feng W, Zhang HP, et al. Shape-selective synthesis and oxygen storage behavior of ceria nanopolyhedra, nanorods, and nanocubes. J Phys Chem B 2005;109:24380–5. https://doi.org/10.1021/jp055584b.

[19] Liu X, Zhou K, Wang L, Wang B, Li Y. Oxygen vacancy clusters promoting reducibility and activity of ceria nanorods. J Am Chem Soc 2009;131:3140–1. https://doi.org/10.1021/ja808433d.

[20] Aneggi E, Wiater D, de Leitenburg C, Llorca J, Trovarelli A. Shape-dependent activity of ceria in soot combustion. ACS Catal 2013;4:172–81. https://doi.org/10.1021/cs400850r.

[21] Zhang T, Chang H, Li K, Peng Y, Li X, Li J. Different exposed facets VO_x/CeO_2 catalysts for the selective catalytic reduction of NO with NH_3. Chem Eng J 2018;349:184–91. https://doi.org/10.1016/j.cej.2018.05.049.

[22] Han J, Meeprasert J, Maitarad P, Nammuangruk S, Shi L, Zhang D. Investigation of the facet-dependent catalytic performance of Fe_2O_3/CeO_2 for the selective catalytic reduction of NO with NH_3. J Phys Chem C 2016;120:1523–33. https://doi.org/10.1021/acs.jpcc.5b09834.

[23] Xie R, Ma L, Sun K, Zhou G, Qu Z, Yan N. Catalytic performance and mechanistic evaluation of sulfated CeO_2 cubes for selective catalytic reduction of NO_x with ammonia. J Hazard Mater 2021;420:126545. https://doi.org/10.1016/j.jhazmat.2021.126545.

[24] Chen J, Zhao W, Wu Q, Mi J, Wang X, Ma L, et al. Effects of anaerobic SO_2 treatment on nano-CeO_2 of different morphologies for selective catalytic reduction of NO_x with NH_3. Chem Eng J 2020;382:122910. https://doi.org/10.1016/j.cej.2019.122910.

[25] Sohn JR, Kim HW. Catalytic and surface properties of ZrO_2 modified with sulfur compounds. J Mol Catal 1989;52:361–74. https://doi.org/10.1016/0304-5102(89)85045-x.

[26] Lian Z, Shan W, Wang M, He H, Feng Q. The balance of acidity and redox capability over modified CeO_2 catalyst for the selective catalytic reduction of NO with NH_3. J Environ Sci (China) 2019;79:273–9. https://doi.org/10.1016/j.jes.2018.11.018.

[27] Yang C, Zhang K, Zhang Y, Peng GJ, Yang M, Wen J, et al. An environmental and highly active Ce/Fe-Zr-SO_4^{2-} catalyst for selective catalytic reduction of NO with NH_3: The improving effects of CeO_2 and SO_4^{2-}. J Environ Chem Eng 2021;9(6). https://doi.org/10.1016/j.jece.2021.106799.

[28] Liu B, Li Q, Du X, Liu B, Yao M, Li Z, et al. Facile hydrothermal synthesis of CeO_2 nanosheets with high reactive exposure surface. J Alloys Compd 2011;509:6720–4. https://doi.org/10.1016/j.jallcom.2011.03.156.

[29] Yin X, Zhang Y, Fang Z, Xu Z, Zhu W. Hydrothermal synthesis of CeO_2 nanorods using a strong base–weak acid salt as the precipitant. Nanosci Methods 2012;1:115–22. https://doi.org/10.1080/17458080.2010.515252.

[30] Wang W, Zhu Q, Qin F, Dai Q, Wang X. Fe doped CeO_2 nanosheets as Fenton-like heterogeneous catalysts for degradation of salicylic acid. Chem Eng J 2018;333:226–39. https://doi.org/10.1016/j.cej.2017.08.065.

[31] Zhuang G, Chen Y, Zhuang Z, Yu Y, Yu J. Oxygen vacancies in metal oxides: recent progress towards advanced catalyst design. Sci China Mater 2020;63(11):2089–118.

[32] Wang M, Ren S, Jiang Y, Su B, Chen Z, Liu W, et al. Insights into co-doping effect of Sm and Fe on anti-Pb poisoning of Mn-Ce/AC catalyst for low-temperature SCR of NO with NH_3. Fuel 2022;319:123763. https://doi.org/10.1016/j.fuel.2022.123763.

[33] Wang Z, Xin Y, Zhang Z, Li Q, Zhang Y, Zhou L. Synthesis of Fe-doped CeO_2 nanorods by a widely applicable coprecipitation route. Chem Eng J 2011;178:436–42. https://doi.org/10.1016/j.cej.2011.10.006.

[34] Zheng X, Li Y, Zheng Y, Shen L, Xiao Y, Cao Y, et al. Highly efficient porous $Fe_xCe_{1-x}O_{2-\delta}$ with three-dimensional hierarchical nanoflower morphology for H_2S-selective oxidation. ACS Catal 2020;10:3968–83. https://doi.org/10.1021/acscatal.9b05486.

[35] Zhang S, Chang CR, Huang ZQ, Li J, Wu Z, Ma Y, et al. High catalytic activity and chemoselectivity of sub-nanometric Pd clusters on porous nanorods of CeO_2 for hydrogenation of nitroarenes. J Am Chem Soc 2016;138:2629–37. https://doi.org/10.1021/jacs.5b11413.

[36] Wang H, Qu Z, Liu L, Dong S, Qiao Y. Promotion of NH_3-SCR activity by sulfate-modification over mesoporous Fe doped CeO_2 catalyst: Structure and mechanism. J Hazard Mater 2021;414:125565. https://doi.org/10.1016/j.jhazmat.2021.125565.

[37] An D, Yang S, Zou W, Sun J, Tan W, Ji J, et al. Unraveling the SO_2 Poisoning Effect over the Lifetime of MeO_x (Me = Ce, Fe, Mn) Catalysts in Low-Temperature NH_3-SCR: Interaction of Reaction Atmosphere with Surface Species. J Phys Chem C 2022;126:12168–77. https://doi.org/10.1021/acs.jpcc.2c02233.

[38] Zhu L, Yao J, Ma G, Cao P, Wu S, Li Z. NH_3-SCR performance and SO_2 resistance comparison of CeO_2 based catalysts with Fe/Mo additive surface decoration. Chem Eng J 2022;428:131372. https://doi.org/10.1016/j.cej.2021.131372.

[39] Gao C, Shi J-W, Fan Z, Gao G, Niu C. Sulfur and Water Resistance of Mn-Based Catalysts for Low-Temperature Selective Catalytic Reduction of NO_x: A Review. Catalysts 2018;8:11–39. https://doi.org/10.3390/catal8010011.

[40] Wu Z, Li M, Howe J, Meyer III HM, Overbury SH. Probing defect sites on CeO_2 nanocrystals with well-defined surface planes by Raman spectroscopy and O_2 adsorption. Langmuir 2010;26:16595–606. https://doi.org/10.1021/la101723w.

[41] El Mendili Y, Bardeau JF, Randrianantoandro N, Gourbil A, Greneche JM, Mercier AM, et al. New evidences of in situ laser irradiation effects on γ-Fe_2O_3 nanoparticles: a Raman spectroscopic study. J Raman Spectrosc 2011;42:239–42. https://doi.org/10.1002/jrs.2762.

[42] Bekana D, Liu R, Li S, Lai Y, Liu JF. Facile fabrication of silver nanoparticle decorated alpha-Fe_2O_3 nanoflakes as ultrasensitive surface-enhanced Raman spectroscopy substrates. Anal Chim Acta 2018;1006:74–82. https://doi.org/10.1016/j.aca.2017.12.003.

[43] Flouty R, Abi-Aad E, Siffert S, Aboukaïs A. Formation of cereous sulphate phase upon interaction of SO_2 with ceria at room temperature. J Therm Anal Calorim 2003;73:727–34. https://doi.org/10.1023/A:1025818127541.

[44] Keller S, Bentrup U, Rabeah J, Brückner A. Impact of dopants on catalysts containing $Ce_{1-x}M_xO_{2-\delta}$ (M = Fe, Sb or Bi) in NH_3-SCR of NO_x – A multiple spectroscopic approach. J Catal 2022;408:453–64. https://doi.org/10.1016/j.jcat.2021.04.026.

[45] Liu F, Shan W, Lian Z, Liu J, He H. The smart surface modification of Fe_2O_3 by WO_x for significantly promoting the selective catalytic reduction of NO_x with NH_3. Appl Catal B: Environ 2018;230:165–76. https://doi.org/10.1016/j.apcatb.2018.02.052.

[46] Trovarelli A. Catalytic properties of ceria and CeO_2-containing materials. Catal Rev 1996;38:439–520. https://doi.org/10.1080/01614949608006464.

[47] Xu Q, Su R, Cao L, Li Y, Yang C, Luo Y, et al. Facile preparation of high-performance Fe-doped Ce–Mn/TiO_2 catalysts for the low-temperature selective catalytic reduction of NO_x with NH_3. RSC Adv 2017;7:48785–92. https://doi.org/10.1039/c7ra07854d.

[48] Graat PCJ, Somers MAJ. Simultaneous determination of composition and thickness of thin iron-oxide films from XPS Fe 2p spectra. Appl Surf Sci 1996;100–101:36–40. https://doi.org/10.1016/0169-4332(96)00252-8.
[49] Huang H, Lan Y, Shan W, Qi F, Xiong S, Liao Y, et al. Effect of sulfation on the selective catalytic reduction of NO with NH_3 over γ-Fe_2O_3. Catal Lett 2013;144:578–84. https://doi.org/10.1007/s10562-013-1174-4.
[50] Romeo M, Bak K, El Fallah J, Le Normand F, Hilaire L. XPS Study of the reduction of cerium dioxide. Surf Interface Anal 1993;20:508–12. https://doi.org/10.1002/sia.740200604.
[51] Bêche E, Charvin P, Perarnau D, Abanades S, Flamant G. Ce 3d XPS investigation of cerium oxides and mixed cerium oxide ($Ce_xTi_yO_z$). Surf Interface Anal 2008;40:264–7. https://doi.org/10.1002/sia.2686.
[52] Kang L, Han L, He J, Li H, Yan T, Chen G, et al. Improved NO_x reduction in the presence of SO_2 by using Fe_2O_3-promoted halloysite-supported CeO_2-WO_3 catalysts. Environ Sci Technol 2019;53:938–45. https://doi.org/10.1021/acs.est.8b05637.
[53] Yu Y, Yi X, Zhang J, Tong Z, Chen C, Ma M, et al. Application of ReO_x/TiO_2 catalysts with excellent SO_2 tolerance for the selective catalytic reduction of NO_x by NH_3. Catal Sci Technol 2021;11:5125–34. https://doi.org/10.1039/d1cy00467k.
[54] Topsoe NY, Topsoe H, Dumesic JA. Vanadia/titania catalysts for selective catalytic reduction (SCR) of nitric-oxide by ammonia: combined temperature programmed in situ FTIR and on-line mass spectroscopy studies. J Catal 1995;151:226–40. https://doi.org/10.1006/jcat.1995.1024.
[55] Vuong TH, Radnik J, Rabeah J, Bentrup U, Schneider M, Atia H, et al. Efficient $VO_x/Ce_{1-x}Ti_xO_2$ catalysts for low-temperature NH_3-SCR: Reaction mechanism and active sites assessed by in situ/operando spectroscopy. ACS Catal 2017;7:1693–705. https://doi.org/10.1021/acscatal.6b03223.
[56] Liu F, Asakura K, He H, Shan W, Shi X, Zhang C. Influence of sulfation on iron titanate catalyst for the selective catalytic reduction of NO_x with NH_3. Appl Catal B: Environ 2011;103:369–77. https://doi.org/10.1016/j.apcatb.2011.01.044.
[57] Yu Y, Wei D, Tong Z, Wang J, Chen J, He C. Rationally engineered ReO_x-$CuSO_4$/TiO_2 catalyst with superior NH_3-SCO efficiency and remarkably boosted SO_2 tolerance: Synergy of acid sites and surface adsorbed oxygen. Chem Eng J 2022;442:136356. https://doi.org/10.1016/j.cej.2022.136356.
[58] Hadjiivanov KI. Identification of neutral and charged N_xO_y surface species by IR spectroscopy. Catal Rev 2000;42:71–144. https://doi.org/10.1081/cr-100100260.
[59] Topsoe NY, Dumesic JA, Topsoe H. Vanadia-titania catalysts for selective catalytic reduction of nitric-oxide by ammonia: studies of acitive sites and formulation of catlaytic cycles. J Catal 1995;151:241–52. https://doi.org/10.1006/jcat.1995.1025.
[60] Takagi M. The mechanism of the reaction between NO_x and NH_3 on V_2O_5 in the presence of oxygen. J Catal 1977;50:441–6. https://doi.org/10.1016/0021-9517(77)90056-2.
[61] Paier J, Penschke C, Sauer J. Oxygen defects and surface chemistry of ceria: quantum chemical studies compared to experiment. Chem Rev 2013;113:3949–85. https://doi.org/10.1021/cr3004949.
[62] Chu K, Cheng YH, Li QQ, Liu YP, Tian Y. Fe-doping induced morphological changes, oxygen vacancies and Ce^{3+}–Ce^{3+} pairs in CeO_2 for promoting electrocatalytic nitrogen fixation. J Mater Chem A 2020;8:5865–73. https://doi.org/10.1039/c9ta14260f.